

Effective-one-body waveform model for noncircularized, planar, coalescing black hole binaries II: high accuracy by improving logarithmic terms in resummations

Alessandro Nagar^{1,2}, Sebastiano Bernuzzi³, Danilo Chiamello¹, Veronica Fantini², Rossella Gamba^{4,5}, Mattia Panzeri^{1,6}, and Piero Retteno¹

¹*INFN Sezione di Torino, Via P. Giuria 1, 10125 Torino, Italy*

²*Institut des Hautes Etudes Scientifiques, 91440 Bures-sur-Yvette, France*

³*Theoretisch-Physikalisches Institut, Friedrich-Schiller-Universität Jena, 07743, Jena, Germany*

⁴*Institute for Gravitation & the Cosmos, The Pennsylvania State University, University Park PA 16802, USA*

⁵*Department of Physics, University of California, Berkeley, CA 94720, USA and*

⁶*Dipartimento di Fisica, Università di Torino, Via P. Giuria 1, 10125 Torino*

Effective-one-body (EOB) models are based on analytical building blocks that, mathematically, are truncated Taylor series with logarithms. These polynomials are usually resummed using Padé approximants obtained first assuming that the logarithms are constant, and then replacing them back into the resulting rational functions. A recent study [1] pointed out that this procedure introduces spurious logarithmic terms when the resummed functions are reexpanded. We therefore explore analytically more consistent resummation schemes. Here we update the `TEOBResumS-DaLi` waveform model for spin-aligned, noncircularized, coalescing black hole binaries by systematically implementing new (still Padé based) resummations for all EOB functions (that is, the potentials and the residual waveform amplitude corrections $\rho_{\ell m}$ up to $\ell = 8$). Once the model is informed by 51 Numerical Relativity simulations (with the usual two flexibility parameters, one in the orbital and one in the spin sector), this new approach proves key in lowering the maximum EOB/NR unfaithfulness $\bar{\mathcal{F}}_{\text{EOBNR}}^{\text{max}}$ for the $\ell = m = 2$ mode (with the Advanced LIGO noise in the total mass range $10 - 200M_{\odot}$) over the whole Simulating eXtreme Spacetimes catalog of 534 waveforms. A median mismatch of 3.418×10^{-4} is achieved, which is a marked improvement on the previous value, 1.06×10^{-3} . The largest value, $\bar{\mathcal{F}}_{\text{EOBNR}}^{\text{max}} \sim 10^{-2}$, is found for an equal-mass, equal-spin simulation with dimensionless spins $\sim +0.994$; only six configurations (all equal-mass, and with equal spins larger than $+0.97$) are above 5×10^{-3} . Results for eccentric binaries are similarly excellent (well below 10^{-2} and mostly around 10^{-3}). For scattering configurations, we find an unprecedented EOB/NR agreement ($< 1\%$) for relatively small values of the scattering angle, though differences progressively increase as the threshold of immediate capture is approached. Our results thus prove that the correct treatment of (apparently) minor analytical details is crucial to obtain highly accurate waveform models for next generation detectors.

I. INTRODUCTION

Numerous works dedicated to the construction of waveform models for coalescing binary black holes (BBHs) have recently called attention to the importance of apparently minor analytical details in the construction of a model [1–3]. In a recent paper [1] (hereafter Paper I), we highlighted the key role of radiation reaction (in analytical, effective-one-body (EOB) resummed form) in obtaining highly Numerical Relativity (NR)-faithful EOB waveforms for non-circularized, spin-aligned, coalescing black hole binaries. More precisely, we focused on two aspects: (i) on the one hand, we found evidence that it could be beneficial to tune the EOB fluxes to NR data in order to decrease the EOB/NR unfaithfulness to the 10^{-4} level; (ii) on the other hand, we showed how a more careful resummation of the functions entering the EOB dynamics, and in particular the treatment of logarithmic-dependent terms, might improve the model in its original form without the need of such additional NR-tuning (see Appendix A of Paper I). In this work, we build upon point (ii). Starting from the model of Paper I, we systematically modify all resummed expression involving Padé approximants, expressions that were previously obtained by treating the $\log(x)$ terms as constants. This results in new resummed expressions for the (A, D) functions entering the conservative dynamics as well as for the residual amplitude corrections $\rho_{\ell m}$ entering the waveform (and radiation reaction). We then inform the model with 51 NR simulations and test its performance on a variety of configurations, including

quasi-circular, eccentric and scattering binaries. The work presented here is part of a strong research effort aimed at generalizing the original `TEOBResumS` model [4, 5] for quasi-circular binaries to more general orbital configurations, including extreme-mass-ratio-inspirals [6–9] or the combined effect of orbital eccentricity and spin precession [10].

The paper is organized as follows: in Sec. II we discuss analytical changes with respect to Paper I, focusing in particular on the new resummed expressions that enter the conservative and nonconservative part of the dynamics. In Sec. III we NR-inform the new model and tests its performance on bound configurations, i.e. either quasi-circular or eccentric inspirals up to merger. Scattering configurations are discussed in Sec. IV, while concluding remarks are collected in Sec. V. The paper is complemented by a technical Appendix A that describes in detail the analytical (approximate) procedure to compute time-derivatives of the phase-space variables needed to obtain the noncircular correction to the waveform and radiation reaction, as originally proposed in Ref. [11].

We adopt the following notations and conventions. The black hole masses are denoted as (m_1, m_2) , the mass ratio is $q = m_1/m_2 \geq 1$, the total mass $M \equiv m_1 + m_2$, the symmetric mass ratio $\nu \equiv m_1 m_2 / M^2$ and the mass fractions $X_i \equiv m_i / M$ with $i = 1, 2$. The dimensionless spin magnitudes are $\chi_i \equiv S_i / m_i^2$ with $i = 1, 2$, and we indicate with $\tilde{a}_0 \equiv \tilde{a}_1 + \tilde{a}_2 \equiv X_1 \chi_1 + X_2 \chi_2$ the effective spin, usually called χ_{eff} in the literature. Unless otherwise stated, we use geometric units with $G = c = 1$.

II. EFFECTIVE-ONE-BODY MODEL AND RESUMMATIONS

Our starting point is the model extensively discussed in Paper I, that is in turn an update of the model of Ref. [2]. To ease the discussion, we thus assume the reader to be familiar with the material discussed in Sec. II of Paper I as well as Sec. II of Ref. [2]. To set the stage, we summarize the analytical changes we implement here and that are the founding blocks of the updated model.

- (i) The (A, D) functions entering the Hamiltonian will be implemented, as anticipated, in a new resummed form, but their starting points are the same PN-expanded versions considered in Paper I, i.e., at formal 5PN order.
- (ii) The $\rho_{\ell m}$ functions are considered as follows: the orbital ρ_{22} is taken at 4PN accuracy and resummed as in Appendix I of Paper I. The other multipoles, up to $\ell = 8$ included, are hybridized with 6PN test-mass information and then resummed with a different treatment of the $\log(x)$ -dependent terms, as explained below.
- (iii) As already pointed out long ago [12], we find that the next-to-next-to-leading order (NNLO) spin-orbit term (3.5PN-accurate) in ρ_{22} (see Refs. [13] and [14] for the PN calculation) has a very large effect that compromises the performance of the model for very large spins. The model turns out to be more flexible (and eventually more accurate and closer to NR waveform data) when this term is discarded and only NLO spin-orbit and spin-spin contributions are retained. For consistency, in doing so we also remove some hybrid-test mass terms that were kept in Paper I building upon the hybridization procedure discussed in Sec. VA of Ref. [15]. Although this term is dropped from the model, we also explore new resummation strategies to incorporate it in the future, including a Borel-Laplace summation.

A. Conservative dynamics

Let us briefly describe the changes in the description of the conservative EOB dynamics with respect to Ref. [2]. The A and D potentials and the Q function are all (formally) considered at 5PN order, their expressions given in Eq.s (2)-(3)-(5) of Ref. [2], respectively. As for Q , we only retain its local-in-time part, and keep it in Taylor-expanded form, without any resummation.

Following Paper I, in A we keep the function $a_6^c(\nu)$ as a free parameter to be informed by NR simulations, while the yet uncalculated 5PN coefficient of the D function is set to zero, $d_5^c = 0$ (see Refs. [16, 17]). The potentials are then resummed following the treatment of the logarithmic terms discussed in Appendix A of Paper I. More precisely, the resummed potentials are obtained by first separating the rational part from the logarithmic-dependent one, and both are separately resummed. With this formal split the

A function reads

$$A = 1 - 2u + 2\nu u^3 + \nu a_3 u^4 + \nu a_5^c u^5 + \nu a_6^c u^6 + \nu(a_5^{\log} u^5 + a_6^{\log} u^6) \log u = A_{\text{poly}}(u) + A_{\log}(u) \log u, \quad (1)$$

and the D function is

$$D = 1 - 6\nu u^2 + \nu d_3 u^3 + \nu d_4^c u^4 + \nu d_5 u^5 + \nu(d_4^{\log} u^4 + d_5^{\log} u^5) \log u = D_{\text{poly}}(u) + D_{\log}(u) \log u, \quad (2)$$

where $u = M/r$ is the inverse radial separation between the two bodies. Then the various polynomial functions are resummed as follows: A_{poly} is replaced by its (3, 3) Padé approximant; in A_{\log} we factor out $a_5^{\log} u^5$ and resum the remainder with a (0, 1) Padé; D_{poly} is replaced by its (3, 2) Padé approximant and in $D_{\log}(u)$ the $d_4^{\log} u^4$ term is factored out and the remainder similarly resummed with a (0, 1) Padé.

B. Waveform and radiation reaction

Let us recall our convention for the multipolar waveform decomposition:

$$h_+ - ih_\times = \frac{1}{D_L} \sum_{\ell=2}^{\infty} \sum_{m=-\ell}^{\ell} h_{\ell m -2} Y_{\ell m}, \quad (3)$$

where D_L is the luminosity distance to the source and $_{-2}Y_{\ell m}$ are the $s = -2$ spin-weighted spherical harmonics. For each multipolar mode, the waveform is factorized as

$$h_{\ell m} = h_{\ell m}^N \hat{h}_{\ell m}, \quad (4)$$

where $h_{\ell m}^N$ is the Newtonian prefactor (given in closed form for the circular case in Ref. [18]) and $\hat{h}_{\ell m}$ is a factorized and resummed PN correction. Following [18], this latter is formally factorized as

$$\hat{h}_{\ell m} = \hat{S}_{\text{eff}} T_{\ell m} e^{i\delta_{\ell m}} (\rho_{\ell m})^\ell, \quad (5)$$

where S_{eff} is the effective source, $T_{\ell m}$ is the tail factor [18], while $\rho_{\ell m}$ and $\delta_{\ell m}$ are the residual amplitude and phase corrections, explicitly computed in the circular limit. The tail factor reads

$$T_{\ell m} = \frac{\Gamma(\ell + 1 - 2i\hat{k})}{\Gamma(\ell + 1)} e^{\pi\hat{k}} e^{2i\hat{k} \log(2kr_0)}. \quad (6)$$

Indicating with E the energy and with Ω the orbital frequency, we have $\hat{k} \equiv mE\Omega$, $k \equiv m\Omega$ and $r_0 = 2/\sqrt{e}$ [19]. For noncircularized dynamics, it is intended that we follow the prescription of Ref. [11], so the Newtonian prefactor is taken in its *generic* form, i.e., with explicit dependence on the time-derivatives of the coordinates as computed along the EOB dynamics.

The $\rho_{\ell m}$'s are then used to construct the radiation reaction force \mathcal{F}_φ according to the prescription of Ref. [2], see Sec. IIC there. In particular, the (2, 2) quasi-circular flux mode is dressed by the general Newtonian prefactor,

again with explicit dependence on time-derivatives of the dynamical variables [11]. More technical details are given in Appendix A, which integrates and completes the information shared in previous works Ref. [2, 11].

The changes with respect to Paper I concern the $\rho_{\ell m}$ functions, that are here resummed differently. Regarding their PN-accuracy, ρ_{22} is taken at full 4PN, as computed in Paper I, while the other functions, up to $\ell = 8$, are taken at 3^{+3} PN order, that is, the 3PN, ν -dependent information is hybridized with test-mass terms so as to reach (formal) 6PN accuracy. The novelty with respect to previous EOB works is the addition of all test-mass terms in $\ell = 7$ and $\ell = 8$ modes, consistently with EOB models valid in the large-mass-ratio limit [20]. The 4PN-accurate ρ_{22} function is resummed according to the procedure of Appendix A of Paper I, starting from Eq. (A7) therein, separating it in a rational part, resummed with a (2, 2) Padé approximant, and a remainder that, after factoring out a $\log(x)$, is a polynomial that is resummed using a (0, 1) Padé approximant. All other modes up to $\ell = 8$ can be formally written as

$$\rho_{\ell m}(x) = p_0(x) + p_1^{\log}(x) \log(x) + p_2^{\log} \log^2(x), \quad (7)$$

where $p_{0,1,2}(x)$ are polynomials in x of the form:

$$p_0(x) = 1 + x + x^2 + x^3 + x^4 + x^5 + x^6, \quad (8)$$

$$p_1^{\log}(x) = x^3 + x^4 + x^5 + x^6, \quad (9)$$

$$p_2^{\log}(x) = x^6. \quad (10)$$

The $p_0(x)$ term is typically resummed with a (4, 2) Padé approximant, except for the (ℓ, m) modes (3, 1), (5, 1), (6, 2), (6, 1), (7, 1), (8, 2) e (8, 1) that are taken in Taylor-expanded form; $p_1^{\log}(x)$, the coefficient of the logarithm, is usually taken in Taylor-expanded form. Exceptions to this rule are the (5, 2), (6, 3), (6, 5), (7, 2), (7, 4), (7, 6), (8, 3), (8, 5) modes, for which we use a P_2^1 approximant, and the (2, 1) and (5, 4) modes, for which we use a P_1^2 approximant. These choices are driven by comparisons with test-mass data (that also involve the black hole spin), and will be detailed in a forthcoming study [21].

1. Spin-dependence: contrasting NLO with NNLO spin-orbit waveform amplitude correction

Following previous work, the spin contribution $\rho_{\ell m}^S$ is simply added to the orbital one, i.e. $\rho_{\ell m} = \rho_{\ell m}^{\text{orb}} + \rho_{\ell m}^S$. As mentioned above, in past models, and in particular in Paper I and Ref. [2], ρ_{22}^S was taken at full NNLO complemented by suitably ν -dressed test-mass terms [15], see Eq. (19) of Paper I. Despite the availability of the NNLO (and beyond) knowledge, the model we discuss here only retains the NLO contributions (both for spin-orbit and for spin-spin) in ρ_{22}^S . This choice is motivated by the fact that, as already mentioned in Ref. [12], the beyond-NLO terms give rather large contributions towards merger that eventually reduce the flexibility of the model and the accuracy of the NR-completion procedure. Despite this, Sec. III below will show that a highly accurate EOB/NR phasing agreement is possible.

Before discussing these results, however, let us explore in some detail the strong field behavior of the function ρ_{22}^S

at NNLO accuracy. The complete ρ_{22} reads

$$\rho_{22} = \rho_{22}^{\text{orb}} + \rho_{22}^S, \quad (11)$$

where

$$\rho_{22}^S = c_{\text{SO}}^{\text{LO}} x^{3/2} + c_{\text{SS}}^{\text{LO}} x^2 + c_{\text{SO}}^{\text{NLO}} x^{5/2} + c_{\text{SS}}^{\text{NLO}} x^3 + c_{\text{SO}}^{\text{NNLO}} x^{7/2}, \quad (12)$$

and the explicit expression of the various coefficients is reported in Eqs. (20)-(23) of Paper I. Fig. 1 compares various representations of ρ_{22} in the extremal situations with $q = 1$ and $\chi_1 = \chi_2 = 1$. The figure illustrates that the effect of the NNLO contribution in the (Taylor-expanded) Eq. (12) is rather large, so that one effectively sees that the function changes shape moving from NLO to NNLO truncation. Such a large difference between NLO and NNLO indicates that one should attempt a resummation. This was the spirit of Ref. [12], that proposed to: (i) factorize the spin-independent part and (ii) resum with certain Padé approximants both the orbital and spin parts. Here we explore a different, more “mathematically natural” procedure. We consider the ρ_{22} global function as the sum of two polynomials, one in integer powers of x and another with semi-integer powers of x , and we resum the two parts separately. Formally, we write the functions as

$$\rho_{22} = \rho_{22}^{\text{orb}} + c_{\text{LO}}^{\text{SS}} x^2 + c_{\text{NLO}}^{\text{SS}} x^3 + c_{\text{SO}}^{\text{LO}} x^{3/2} (1 + c_{\text{nlo}} x + c_{\text{nnlo}} x^2) \quad (13)$$

where $c_{\text{nlo}} \equiv c_{\text{SO}}^{\text{NLO}}/c_{\text{SO}}^{\text{LO}}$ and $c_{\text{nnlo}} \equiv c_{\text{SO}}^{\text{NNLO}}/c_{\text{SO}}^{\text{LO}}$. The function $(1 + c_{\text{nlo}} x + c_{\text{nnlo}} x^2)$ is then resummed as a (1, 1) Padé approximant. For the even-in-spin part we can adopt two different procedures. On the one hand, we can resum just ρ_{22}^{orb} as discussed above, with no further treatment applied to the spin-spin terms. On the other hand, the spin-spin terms can be incorporated in the rational part ρ_{22}^{orb} and resummed together with the nonspinning ones via the (2, 2) Padé approximant. Fig. 1 also compares these two approaches, indicating that they are broadly consistent, though fractional differences of a few percent can be appreciated at large frequencies. In a forthcoming study dealing with the fluxes in the test-mass limit [21], we will show that treating separately integer and semi-integer powers of x yields a better agreement with the numerical data and thus this choice should be a priori preferred also in the comparable mass case. Fig. 1 shows that, even when resummed, the NNLO expressions remain larger than the the NLO *nonresummed* version, and thus their use will eventually prevent us from obtaining an EOB waveform model as NR-faithful as the one we will discuss in the next section. Evidently this is true keeping the same treatment of the spin-orbit interaction in the conservative part of the dynamics. We cannot exclude that a different approach to the spin-orbit sector could allow us to easily use the resummed expression. Additional investigations aimed at exploring this possibility are postponed to future work.

To gain more insight on the robustness of our Padé approximants in x -space in view of future applications, it is also instructive to explore the outcome of applying Borel summation to the spin-orbit terms. Although Borel summation is commonly used to resum divergent power series [22, 23], it can also be employed in combination with Padé approximation to study (possibly convergent) power series. We refer to this resummation paradigm as Borel–Padé–Laplace (BPL). This scheme requires three steps:

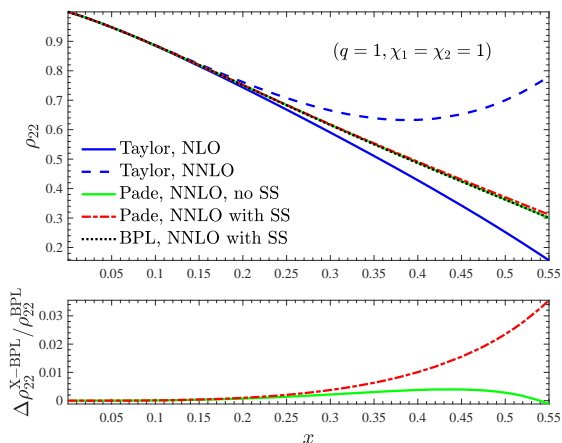


FIG. 1. Comparing resummed and nonresummed expressions of the spin part of ρ_{22} , ρ_{22}^S , Eq. (12). The plot highlights the mutual consistency between three different resummed expressions for ρ_{22}^S , including the Borel-Padé-Laplace (BPL). Bottom panel: relative differences between the two Padé resummed expressions and the BPL. See text for details.

- (i) The first step is given by the Borel transform $\mathcal{B}: x^\alpha \mathbb{C}[[x]] \rightarrow s^\alpha \mathbb{C}[[s]]$. By definition, for every $n = 1, 2, \dots$ and $\alpha \in \mathbb{Q} \setminus \mathbb{Z}^{\times 1}$ the Borel transform maps monomials $x^{n+\alpha+1}$ to monomials $\frac{s^{n+\alpha}}{\Gamma(n+\alpha+1)}$, and it is extended by countable linearity to formal power series

$$\mathcal{B}\left(x^\alpha \sum_{n=0}^{\infty} a_n x^n\right) = s^\alpha \sum_{n=1}^{\infty} a_n \frac{s^{n-1}}{\Gamma(n+\alpha)}.$$

- (ii) The second step consists of taking a Padé approximant in s -space. If fractional powers of s are present, it is preferable to use Padé on the integral part after the factorization of the lowest fractional exponent (see Eq. (17)).
- (iii) The third step is given by the Laplace transform \mathcal{L} which acts on locally integrable exponentially decaying functions on the positive reals and gives real-analytic functions,

$$[\mathcal{L}\hat{f}](x) := \int_0^{+\infty} e^{-\frac{x}{s}} \hat{f}(s) ds. \quad (14)$$

Notice that the choice of Padé approximant in s -space should be made so that no poles lie on the positive reals, as it will otherwise not be possible to perform the Laplace transform. Still, even if every choice of Padé approximant did have poles on the positive reals, it would yet be possible to take the so called median resummation (see for instance Eq. (214) in Ref. [24]), by extending s to be a complex variable.

To cross check the Padé resummation of the semi-integer powers part of ρ_{22}^S in Eq. (12), we implement a

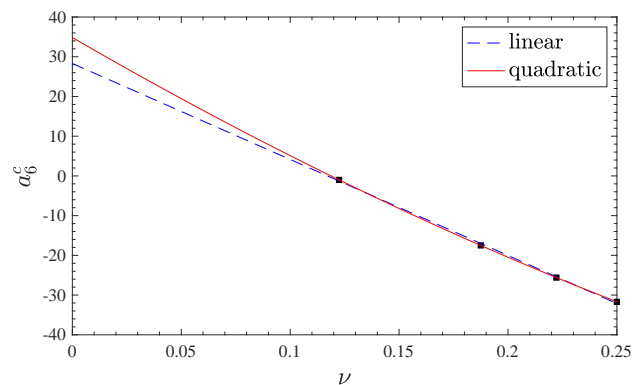


FIG. 2. NR-informed values of a_6^c (points) and their fits. The quadratic function, Eq. (19), yields an EOB dynamics that is NR-faithful also for $q > 6$ ($\nu \lesssim 0.122$).

BPL resummation. As an illustrative example, let us consider a function of the form:

$$f = f_{3/2} x^{3/2} + f_{5/2} x^{5/2} + f_{7/2} x^{7/2}. \quad (15)$$

Then, its Borel transform is

$$[\mathcal{B}f](s) = f_{3/2} \frac{s^{1/2}}{\Gamma(\frac{3}{2})} + f_{5/2} \frac{s^{3/2}}{\Gamma(\frac{5}{2})} + f_{7/2} \frac{s^{5/2}}{\Gamma(\frac{7}{2})}. \quad (16)$$

Since there are fractional exponents, we use a Padé (1,1) on the polynomial

$$s^{-\frac{1}{2}} [\mathcal{B}f](s) = \frac{f_{3/2}}{\Gamma(\frac{3}{2})} + \frac{f_{5/2}}{\Gamma(\frac{5}{2})} s + \frac{f_{7/2}}{\Gamma(\frac{7}{2})} s^2, \quad (17)$$

and we obtain a rational function

$$\hat{f}(s) = s^{\frac{1}{2}} \frac{p_0 + p_1 s}{1 + q_1 s}, \quad (18)$$

for some coefficients p_0, p_1, q_1 . The last step consists of taking the Laplace transform of \hat{f} , which gives a real-analytic function in the original x -space. The BPL-resummed spin-orbit part is then added to the orbital part resummed in x -space, that also incorporates the spin-spin terms $c_{SS}^{LO} x^2$ and $c_{SS}^{NLO} x^3$ in the (2, 2) Padé approximant. The result is displayed as a black solid line in the top panel of Fig. 1. The bottom panel shows the fractional difference between each Padé resummed expression and the BPL one, i.e. $\Delta \rho_{22}^{X-BPL} \equiv \rho_{22}^X - \rho_{22}^{BPL}$ where X can be either one of the two Padé. The consistency between the three resummed expressions is evident, although the BPL one is found to be closer to the Padé-resummed one with the spin-spin terms simply added instead to the one with them incorporated within the Padé, as a priori expected. In any case, this comparison indicates that the BPL procedure is a useful tool to cross-validate Padé resummations in x -space in the absence of other validation tools (e.g., exact data).

III. BINARIES ON BOUND ORBITS

A. Informing the model using NR simulations

The determination of a_6^c and c_3 follows the usual procedure highlighted in Paper I, that consists in finding the

¹ We denote by \mathbb{Q} the set of rationals, and by \mathbb{Z}^{\times} the set of non zero integers.

TABLE I. Coefficients for the fit of c_3 given by Eq. (20).

Model	$c_3^- \equiv p_0 \left(1 + n_1 \tilde{a}_0 + n_2 \tilde{a}_0^2 + n_3 \tilde{a}_0^3 + n_4 \tilde{a}_0^4 \right) / (1 + d_1 \tilde{a}_0)$ $c_3^\neq \equiv \left(p_1 \tilde{a}_0 + p_2 \tilde{a}_0^2 + p_3 \tilde{a}_0^3 \right) \sqrt{1 - 4\nu} + p_4 \tilde{a}_0 \nu \sqrt{1 - 4\nu} + \left(p_5 \tilde{a}_{12} + p_6 \tilde{a}_{12}^2 \right) \nu^2$											
TEOBResumS*	p_0	n_1	n_2	n_3	n_4	d_1	p_1	p_2	p_3	p_4	p_5	p_6
Dali _{newlogs}	41.683	-1.656	0.967	-0.171	-0.0456	-0.688	12.2697	-2.5116	3.4525	-56.4450	67.7644	-93.5733

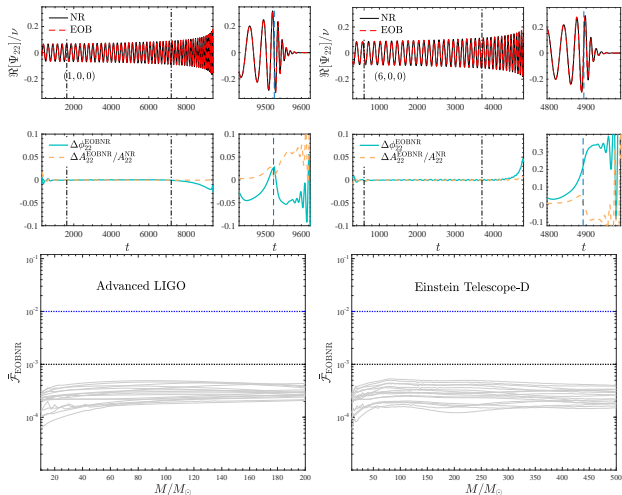


FIG. 3. Nonspinning case. Top panels: two illustrative time-domain EOB/NR phasings for the $\ell = m = 2$ waveform mode. The dash dotted vertical lines in the left part of each panel indicate the alignment interval, while the dashed line in the right panel show the merger time, i.e. the peak of the NR waveform. Bottom panels: EOB/NR unfaithfulness for all SXS nonspinning datasets available (including the $q = 15$ case, see Fig. 4) with both the Advanced-LIGO and ET-D [25–27] sensitivity designs. The small phase differences accumulated up to merger yield $\mathcal{F}_{\text{EOB/NR}}^{\text{max}} \sim 10^{-4}$. The largest value for the Advanced-LIGO sensitivity is 4.9×10^{-4} , obtained for $q = 10$.

values of the parameters that minimize the accumulated phase difference at merger (when possible) when the EOB and NR waveforms are aligned in the time-domain during the early inspiral. In particular, one does so being careful that the phase difference is flat during the inspiral and a monotonically decreasing (or increasing) function of time when approaching merger. We find that to determine a_6^c it was sufficient to use only 4 datasets², with mass ratios $q = (1, 2, 3, 6)$ with corresponding values $a_6^c = (-31.7, -25.6, -17.5, -1)$. The values of $a_6^c(\nu)$ (see Fig. 2) are accurately fitted by the following quadratic function of ν

$$a_6^c(\nu) = 208.19\nu^2 - 318.26\nu + 34.85. \quad (19)$$

Although at first sight the points are approximately disposed along a straight line (and can be fitted as $a_6^{c-\text{linear}}(\nu) = 8.3053 - 241.662\nu$), one is actually sensitive to the quadratic term in Eq. 19, and removing it yields

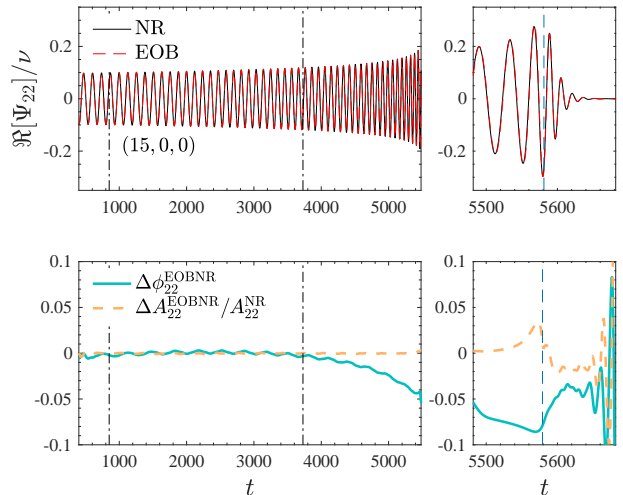


FIG. 4. EOB/NR time domain phasing for $q = 15$, nonspinning. It is remarkable that the model performs so well for such a large mass ratio, even if the function $a_6^c(\nu)$ was determined using only NR data with mass ratios $q = (1, 2, 3, 6)$.

large phase differences at merger for large mass ratios, e.g. ~ 1.9 rad for $q = 9.5$. We will come back to this point when discussing the performance of the model, Sec. III B below.

The function c_3 is determined using the same SXS configurations used in Paper I, that, for completeness, are listed in Tables IV–V together with the first-guess values of c_3 that are suitably fitted. The NR-informed analytical expression for c_3 is obtained using the same functional form and the same set of SXS NR data of Ref. [3]. It reads:

$$c_3(\nu, \tilde{a}_0, \tilde{a}_{12}) = c_3^- + c_3^\neq, \quad (20)$$

where

$$c_3^- \equiv p_0 \frac{1 + n_1 \tilde{a}_0 + n_2 \tilde{a}_0^2 + n_3 \tilde{a}_0^3 + n_4 \tilde{a}_0^4}{1 + d_1 \tilde{a}_0} \quad (21)$$

$$c_3^\neq \equiv \left(p_1 \tilde{a}_0 + p_2 \tilde{a}_0^2 + p_3 \tilde{a}_0^3 \right) \sqrt{1 - 4\nu} + p_4 \tilde{a}_0 \nu \sqrt{1 - 4\nu} + \left(p_5 \tilde{a}_{12} + p_6 \tilde{a}_{12}^2 \right) \nu^2, \quad (22)$$

The coefficients of the fit are listed in Table I.

B. Testing: quasi-circular and eccentric binaries

We begin the comprehensive testing of the model with the quasi-circular configurations. As usual, EOB and NR waveforms are compared both computing the EOB/NR

² Precisely, the dataset we used are SXS:BBH:0180, SXS:BBH:0169, SXS:BBH:0168 and SXS:BBH:0166.

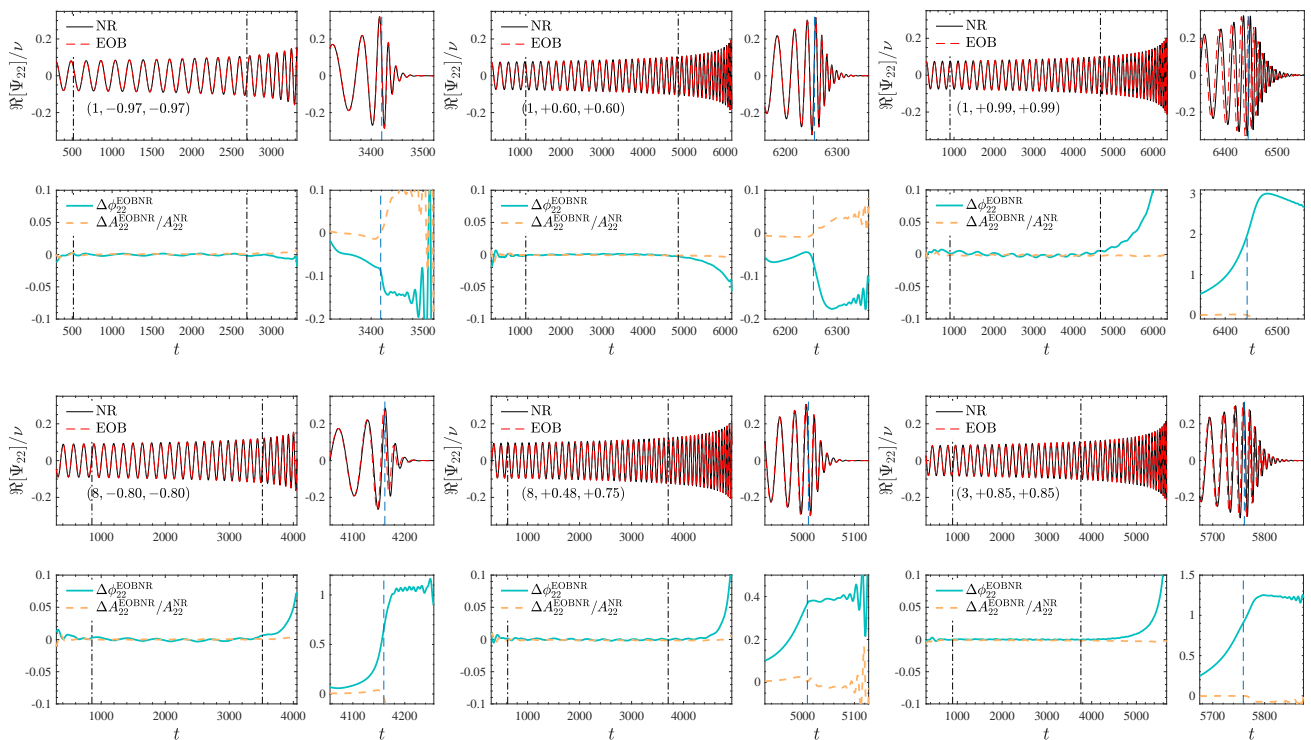


FIG. 5. EOB/NR time-domain phasings for a few illustrative, spin-dependent, configurations all over the parameter space. The largest EOB/NR dephasings are found around the equal-mass, large positive spin corner. Dephasings at merger ~ 2 rad for $(1, +0.99, +0.99)$ yield maximum unfaithfulness values $\sim 10^{-2}$; by contrast, dephasings ~ 0.1 rad yield $\bar{\mathcal{F}}_{\text{EOBNR}}^{\text{max}} \sim 10^{-4}$, see Fig. 6

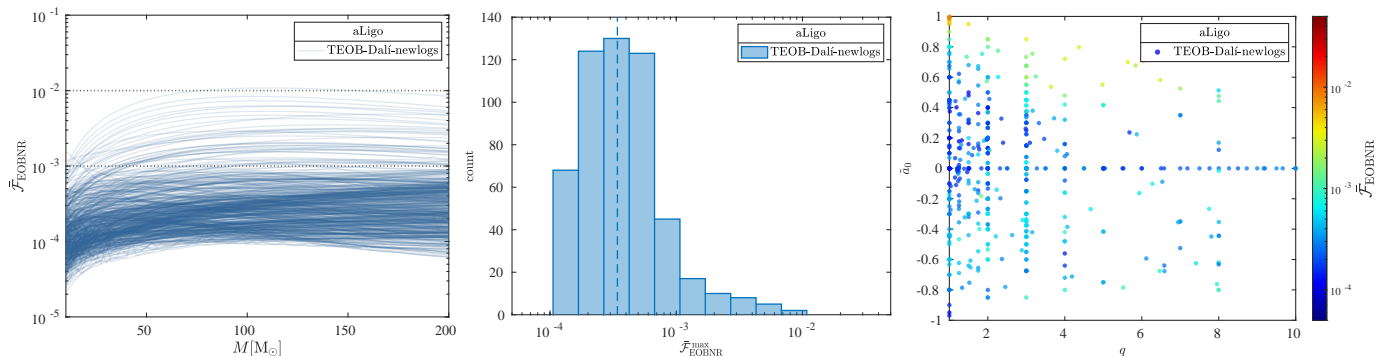


FIG. 6. Left panel: EOB/NR unfaithfulness for the $\ell = m = 2$ mode versus the binary total mass M all over the 531 spin-aligned simulations of the SXS catalog. Middle panel: distribution of the maximum unfaithfulness $\bar{\mathcal{F}}_{\text{EOBNR}}^{\text{max}}$, whose median is 3.418×10^{-4} , vertical line in the middle panel. This is the smallest value ever obtained for an EOB model. Right panel: $\bar{\mathcal{F}}_{\text{EOBNR}}^{\text{max}}$ versus (\tilde{a}_0, q) . The EOB/NR disagreement is at most $\sim 1.08 \times 10^{-2}$, for $q = 1$ and $\chi_1 = \chi_2 = 0.994$. Only 6 configurations have $\bar{\mathcal{F}}_{\text{EOBNR}}^{\text{max}} > 0.5\%$, and are all equal mass and equal spin ones with $\chi_1 = \chi_2 \gtrsim 0.97$. Note the improvement with respect to Fig. 11 of Ref. [1] despite the absence of NR-tuning of radiation reaction.

phase difference in the time domain and the EOB/NR unfaithfulness for a given detector noise. This quantity, addressed as $\bar{\mathcal{F}}$, is defined as follows. Given two waveforms (h_1, h_2) , $\bar{\mathcal{F}}$ is a function of the total mass M of the binary:

$$\bar{\mathcal{F}}(M) \equiv 1 - \mathcal{F} = 1 - \max_{t_0, \phi_0} \frac{\langle h_1, h_2 \rangle}{\|h_1\| \|h_2\|}, \quad (23)$$

where (t_0, ϕ_0) are the initial time and phase. We used $\|h\| \equiv \sqrt{\langle h, h \rangle}$, and the inner product between two waveforms is defined as $\langle h_1, h_2 \rangle \equiv 4\Re \int_{f_{\text{min}}^{\text{NR}}(M)}^{\infty} \tilde{h}_1(f) \tilde{h}_2^*(f) / S_n(f) df$, where $\tilde{h}(f)$ denotes the Fourier transform of $h(t)$, $S_n(f)$ is the detector power spectral density (PSD), and $f_{\text{min}}^{\text{NR}}(M) = \hat{f}_{\text{min}}^{\text{NR}} / M$ is the

initial frequency of the NR waveform at highest resolution, i.e. the frequency measured after the junk-radiation initial transient. For S_n , in our comparisons we use either the zero-detuned, high-power noise spectral density of Advanced LIGO [28] or the predicted sensitivity of Einstein Telescope [26, 27]. Waveforms are tapered in the time-domain to reduce high-frequency oscillations in the corresponding Fourier transforms.

Following the same logic of Paper I, it is instructive to focus first on nonspinning binaries. The top panel of Fig. 3 reports time-domain phasings in terms of the Regge-Wheeler-Zerilli [32] normalized modes, $\Psi_{\ell m} = h_{\ell m} / \sqrt{(\ell+2)(\ell+1)\ell(\ell-1)}$, for two selected datasets

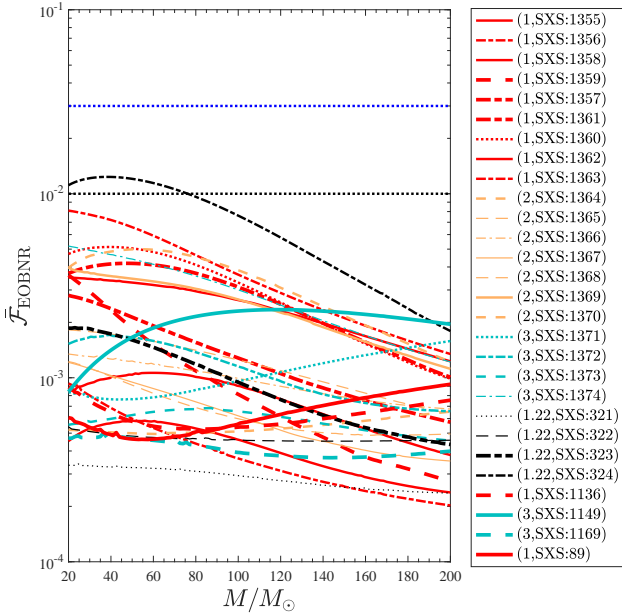


FIG. 7. EOB/NR unfaithfulness for the $\ell = m = 2$ mode calculated over the 28 publicly available SXS eccentric simulations.

TABLE II. Comparison between EOB and NR scattering angle for nonspinning binaries from the sequence of Ref. [29] (fixed energy, varying angular momentum, first 10 rows) and from Ref. [30] (fixed angular momentum and varying energy, last 5 rows).

#	$E_{\text{in}}^{\text{NR}}/M$	$J_{\text{in}}^{\text{NR}}/M^2$	χ^{NR}	$\chi_{\text{newlogs}}^{\text{EOB}}$	$\Delta\chi_{\text{newlogs}}^{\text{EOBNR}} [\%]$
1	1.0225555	1.099652	305.8(2.6)	<i>plunge</i>	...
2	1.0225722	1.122598	253.0(1.4)	310.780	22.83
3	1.0225791	1.145523	222.9(1.7)	252.790	13.41
4	1.0225870	1.214273	172.0(1.4)	181.361	5.44
5	1.0225884	1.260098	152.0(1.3)	157.392	3.55
6	1.0225907	1.374658	120.7(1.5)	122.330	1.35
7	1.0225924	1.489217	101.6(1.7)	102.122	0.514
8	1.0225931	1.603774	88.3(1.8)	88.471	0.193
9	1.0225938	1.718331	78.4(1.8)	78.426	0.033
10	1.0225932	1.832883	70.7(1.9)	70.631	0.097
11	1.035031	1.1515366	307.13(88)	<i>plunge</i>	...
12	1.024959	1.151845	225.54(87)	263.936	17.02
13	1.0198847	1.151895	207.03(99)	224.801	8.59
14	1.0147923	1.151918	195.9(1.3)	204.311	4.28
15	1.0045678	1.1520071	201.9(4.8)	202.774	0.43

with $q = 1$ and $q = 6$. We focus only on the $\ell = m = 2$ mode, that is decomposed in phase and amplitude as $\Psi_{22} = A_{22}^{-i\phi_{22}}$. Considering first the equal-mass case, we highlight that the phase difference accumulated up to merger is just $\Delta\phi_{22}^{\text{EOBNR}} \equiv \phi_{22}^{\text{EOB}} - \phi_{22}^{\text{NR}} \sim -0.05$ rad, yielding $\bar{\mathcal{F}}_{\text{EOBNR}} \sim 10^4$, with $\bar{\mathcal{F}}_{\text{EOBNR}}^{\text{max}} \sim 4.3 \times 10^{-4}$. For $q = 6$, the cumulative dephasing is ~ 0.2 rad, yielding only $\bar{\mathcal{F}}_{\text{EOBNR}}^{\text{max}} = 2.68 \times 10^{-4}$. The time evolution of $\Delta\phi_{22}^{\text{EOBNR}}$ is qualitatively compatible with, though quantitatively better than, the corresponding one shown in Fig. 10 of Paper I. This one was however relying on an ad-

TABLE III. Comparison between EOB and the (average) NR scattering angle for some of the equal-mass, spin-aligned, configurations of Ref. [31]. All datasets share the same initial angular momentum $J_{\text{in}}^{\text{NR}}/M^2 = 1.14560$. Datasets are ordered according to the values of the effective spin \tilde{a}_0 . The remarkable EOB/NR agreement obtained for small values of the scattering angle degrades progressively as the threshold of direct capture is approached.

χ_1	χ_2	\tilde{a}_0	$E_{\text{in}}^{\text{NR}}/M$	χ^{NR}	$\chi_{\text{newlogs}}^{\text{EOB}}$	$\Delta\chi_{\text{newlogs}}^{\text{EOBNR}} [\%]$
-0.30	-0.30	-0.30	1.02269	<i>plunge</i>	<i>plunge</i>	...
-0.25	-0.25	-0.25	1.02268	367.55	<i>plunge</i>	...
-0.23	-0.23	-0.23	1.02267	334.35	<i>plunge</i>	...
-0.20	-0.20	-0.20	1.02266	303.88	<i>plunge</i>	...
-0.15	-0.15	-0.15	1.02265	272.60	<i>plunge</i>	...
-0.10	-0.10	-0.10	1.02265	251.03	314.63	25.34
-0.05	-0.05	-0.05	1.02264	234.57	277.34	18.24
0.0	0.0	0.0	1.02264	221.82	253.19	14.14
+0.80	-0.80	0.0	1.02309	221.68	255.85	15.42
+0.20	-0.20	0.0	1.02266	221.82	253.27	14.18
+0.10	+0.10	+0.10	1.02265	202.61	221.67	9.41
+0.80	-0.50	+0.15	1.02294	198.99	211.06	6.06
+0.70	-0.30	+0.20	1.02284	190.41	201.34	5.74
+0.20	+0.20	+0.20	1.02266	187.84	200.94	6.98
+0.30	+0.30	+0.30	1.02269	176.59	185.84	5.24
+0.60	0.0	+0.30	1.02276	177.63	186.01	4.72
+0.40	+0.40	+0.40	1.02274	167.54	174.13	3.93
+0.80	+0.20	+0.50	1.02288	162.07	164.79	1.68
+0.60	+0.60	+0.60	1.02288	154.14	156.81	1.73
+0.80	+0.50	+0.65	1.02295	152.30	153.41	0.73
+0.80	+0.80	+0.80	1.02309	145.36	144.37	0.68

hoc NR-calibration of the radiation reaction through the ρ_{22} function. This calibration is not needed now, and the improved performance is fully due to the new treatment of the logarithmic terms. Consistently, in the bottom panel of the figure we report the computation of $\bar{\mathcal{F}}_{\text{EOBNR}}$, as a function of the total mass M , with either the Advanced LIGO noise (left panel) or the ET predicted sensitivity curve (right panel). The figure is similarly consistent with the bottom panels of Fig. 10 of Paper I. Given how small the accumulated phase difference is along the full evolution, it seems hard to further improve the model in this regime without a more stringent estimate of the NR error, which the model might be grazing now. For $q = 6$ we accepted a phase difference larger than the equal-mass case (a slightly different value of a_6^{eff} could have yielded an even smaller value of $\Delta\phi_{22}^{\text{EOBNR}}$) with the understanding that for such large mass ratio the NR uncertainty might be slightly larger than for the $q = 1$ case. For SXS datasets the NR uncertainty is usually estimated comparing two different resolutions as given in the public catalog, and this typically yields values of NR-NR unfaithfulness of the order of $10^{-4} - 10^{-5}$ (see for example Sec. 4 in Ref. [33], or the left panel of Fig. 2 in Ref. [34]) i.e. still mostly below the current EOB/NR unfaithfulness level, but comparable for some configurations. Nonetheless, it is worth stressing that $\Delta\phi_{22}^{\text{EOBNR}}$ remains of the same order *also* for larger

mass ratios (not used to determine a_6^c) and most notably it is even smaller for $q = 15$, as illustrated in Fig. 4. This is a remarkable fact because it shows that the model presented here is very accurate also *outside* the region of the parameter space used to determine a_6^c and thus its predictive power (and accuracy) generally looks stronger than its previous avatars. The waveform was tested also versus NR simulations with large mass ratios up to $q = 128$ [35]. The consistency through merger and ringdown is analogous to the one obtained in Ref. [36] for the quasi-circular **TEOBResumS-GIOTTO** model.

Some additional illustrative phasing comparisons for spinning binaries are shown in Fig. 5. In general, for large, positive spins the tuning of c_3 is ineffective in further reducing the phase difference during the late inspiral, that for $(1, +0.99, +0.99)$ is ~ 2 rad. As shown above, the use of the NNLO spin-orbit correction in ρ_{22}^S , even in resummed form, increases the waveform amplitude. This, in turn, further accelerates the inspiral, yielding an even larger phase difference at merger for large, positive, spins. The consistency found between the Padé resummed expression and the one obtained using Borel-Padé-Laplace technique suggests that the analytical description of the spin-orbit sector should be reconsidered. We also mention, in passing, that for large-positive spins the dynamics might be affected by the angular momentum flux absorbed by the two black holes [37, 38]. This effect is incorporated at leading order in the model from Ref. [4], but a careful assessment of its properties as well as the impact of the most recent analytical results [39] is still lacking, and careful investigations within the EOB model are currently in progress.

Fig. 6 gives a global overview of the performance of the model, tested over the full SXS catalog of spin-aligned NR simulations [33]. The left panel shows $\bar{\mathcal{F}}_{\text{EOBNR}}$ versus the total mass M of the binary in the range $10 - 200M_\odot$, while the right panel shows $\bar{\mathcal{F}}_{\text{EOBNR}}^{\text{max}}$. The plot clearly indicates how the model performance degrades for large positive spins, with the worst performance obtained for the analytically most demanding cases, i.e. equal mass, nearly extremal spins. This should not however distract from the remarkable fact that $\bar{\mathcal{F}}_{\text{EOBNR}}^{\text{max}}$ is of the order of 10^{-3} (or below) for most of the dataset, with the median of the mismatch distribution being $\bar{\mathcal{F}}_{\text{EOBNR}}^{\text{max, median}} = 3.418 \times 10^{-4}$. This is smaller than the $\bar{\mathcal{F}}_{\text{EOBNR}}^{\text{max, median}} = 1.06 \times 10^{-3}$ obtained in Paper I while NR-tuning *also* the radiation reaction, and comparable to the values obtained with the standard quasi-circular EOB models **TEOBResumS-GIOTTO** [3] or **SEOBNRv5** [40]. It must be said however that these two models are slightly better, especially for high spins, since for **TEOBResumS-GIOTTO** [3] we have $\bar{\mathcal{F}}_{\text{EOBNR}}^{\text{max}} \lesssim 10^{-3}$ and for **SEOBNRv5** [40] $\bar{\mathcal{F}}_{\text{EOBNR}}^{\text{max}} \lesssim 3 \times 10^{-3}$. We also remark that only six, equal-mass configurations with $\chi_1 = \chi_2 \gtrsim 0.97$ yield $\bar{\mathcal{F}}_{\text{EOBNR}}^{\text{max}} > 5 \times 10^{-3}$, i.e. SXS:BBH:0157, SXS:BBH:0158, SXS:BBH:0172, SXS:BBH:0177, SXS:BBH:0178, SXS:BBH:1124. Focusing on the middle panel of Fig. 6, it is also worth noting that, modulo the high spin case, the most of the smallest value of $\bar{\mathcal{F}}_{\text{EOBNR}}^{\text{max}}$ are obtained for moderately high, positive, spins with mass ratio in the range $1 \leq q \leq 4$. This is the consequence that most of the datasets used to NR-inform c_3 have $q \lesssim 4$ and $\tilde{a}_0 > 0$ (see Table V), just 9 have $\tilde{a}_0 < 0$. On the one hand, this fact shows that the ana-

lytical spin sector of **TEOBResumS-Da1í** is very robust and predictive as it can predict the waveforms rather correctly even in the absence of many anchor points on part of the parameter space. On the other hand, it suggests that the performance in the $\tilde{a}_0 < 0$ part of the (\tilde{a}_0, q) plane could be improved further (say at the 10^{-4} level) by just anchoring the determination of c_3 to another few datasets with $1 \leq q \leq 4$ and $\tilde{a}_0 < 0$. Since our purpose here is to explore here mainly the effect of the new analytic treatment of the logarithmic terms in the various function without changing the NR information, we postpone this to future work.

Finally, the EOB/NR unfaithfulness comparisons for eccentric binaries are shown in Fig. 7. As usual, the model is compared with the only 28 publicly available SXS datasets [41], whose binary properties (mass ratio and spins) can be found in Table IV of Paper I. The performance is much improved with respect to Paper I, see Fig. 8 (or Fig. 12) therein, except for the case SXS:BBH:324, corresponding to $(1.22, +0.33, -0.44)$ that is characterized by the largest initial NR eccentricity at apastron ($e_{\omega_a} \sim 0.20$) and a rather noisy (and possibly slightly inaccurate) inspiral. The initial data were slightly retuned with respect to previous work to compensate for the various analytical modifications that were implemented in the model concerning the inspiral. Considering that the choice of initial data can probably be improved further [42], the performance is already much better than in Paper I. In particular, it is worth to remark that for SXS:BBH:1149, corresponding to $(3, +0.70, +0.60)$ we have $\bar{\mathcal{F}}_{\text{EOBNR}}^{\text{max}} \sim 2 \times 10^{-3}$, a result that was out of reach with previous models (except when NR-tuning the radiation reaction).

IV. SCATTERING CONFIGURATIONS

Let us finally analyze scattering configurations, focusing on the same equal-mass data used in Paper I. The NR data are taken from Refs. [29] (fixed energy, varying angular momentum, nonspinning), Ref. [30] (fixed angular momentum, varying energy, nonspinning) and Ref. [31] (fixed energy and angular momentum while varying the initial spins). The NR and EOB data are compared in Tables II and III. Each table reports the initial values of the NR energy $E_{\text{in}}^{\text{NR}}/M$ and angular momentum $J_{\text{in}}^{\text{NR}}/M^2$, the NR value χ^{NR} , the EOB value $\chi_{\text{newlogs}}^{\text{EOB}}$ as well as the fractional difference $\Delta\chi_{\text{newlogs}}^{\text{EOBNR}} \equiv (\chi_{\text{newlogs}}^{\text{EOB}} - \chi^{\text{NR}})/\chi^{\text{NR}}$. The most interesting finding is that we obtained an excellent (and unprecedented) EOB/NR agreement for the smallest values of the scattering angle, that is well below the 1% level for several configurations, notably datasets #9, #10 and #15 in Table II or the last rows of Table III. Comparing with the corresponding data in Tables V and VI of Paper I we see the improved EOB/NR consistency obtained now thanks to the more correct analytic treatment of all logarithmic terms. The case with $\chi_1 = \chi_2 = +0.80$ is particularly remarkable. It yields $\Delta\chi_{\text{newlogs}}^{\text{EOBNR}} \sim 0.6\%$, to be contrasted with the $\sim 5\%$ relative difference obtained in Paper I, despite using an NR-calibrated flux.

A few considerations are in order. First, this finding is a remarkable consistency test (and the first of its kind) between the EOB dynamics for bound and unbound configurations. Second, it exemplifies the fact that suboptimal

TABLE IV. First-guess values for c_3 for equal-mass, equal-spin configurations. They are used to determine $c_3^{\bar{}}$ in Eq. (20).

#	ID	(q, χ_1, χ_2)	\tilde{a}_0	c_3^{newlogs}
1	BBH:1137	(1, -0.9692, -0.9692)	-0.9692	90.5
2	BBH:0156	(1, -0.9498, -0.9498)	-0.95	90.0
3	BBH:2086	(1, -0.80, -0.80)	-0.80	81.0
4	BBH:2089	(1, -0.60, -0.60)	-0.60	69.5
5	BBH:2089	(1, -0.20, -0.20)	-0.60	51.0
6	BBH:0150	(1, +0.20, +0.20)	+0.20	33.5
7	BBH:0170	(1, +0.4365, +0.4365)	+0.20	26.5
8	BBH:2102	(1, +0.60, +0.60)	+0.60	22.5
9	BBH:2104	(1, +0.80, +0.80)	+0.80	17.5
10	BBH:0160	(1, +0.8997, +0.8997)	+0.8997	14.9
11	BBH:0157	(1, +0.949586, +0.949586)	+0.949586	14.0
12	BBH:0177	(1, +0.989253, +0.989253)	+0.989253	13.0

(if not really incorrect) analytic choices *cannot* be compensated by suitable calibrations to NR results. Last, the excellent EOB/NR agreement for (relatively) small values of the scattering angle is contrasted with its progressive worsening as the scattering angle increases, with incorrect analytical predictions as the threshold of direct capture is approached. This is consistent with a very recent EOB/NR analysis [43] that used NR simulations to define the basin of initial conditions that eventually outline the region of transition between scattering and dynamical capture. Our findings indicate that the strong-field description of the EOB potentials in scattering configurations should be improved. In other words, in terms of the effective potential A the description of the circular *unstable* orbits needs to be modified. At the same time, the EOB dynamics also depends on the potentials D and Q and small changes in their strong-field behavior may give rise to visible differences. Let us recall in this respect that, though D is resummed, Q is not and we are considering only its local part. A systematic analysis of the strong-field behavior of (D, Q) (and possibly their resummations) might improve the EOB/NR agreement for the scattering angle. The role of D (notably working up to 6PN) was partly investigated in Ref.s [44] and [3]. These studies should be updated with the current choice of radiation reaction and presented systematically in future work.

V. CONCLUSIONS

Systematic biases related to incorrect models threaten to limit our ability to extract astrophysical information from GW signals [45–47]. Building on the insight gained in previous work [1] we have presented here a new and improved avatar of the `TEOBResumS-DaLi` model for generic, spin-aligned binaries that is based on analytically more consistent Padé resummation schemes. More precisely, the logarithms that appear in both the conservative and nonconservative sectors of the model are factorized and their polynomial coefficients are Padé resummed whenever needed. For what concerns the radiation reaction, this procedure is applied on all multipoles up to $\ell = 8$.

TABLE V. First-guess values for c_3 for the unequal-spin and unequal-mass configurations. They are used to determine c_3^{\neq} in Eq. (20).

#	ID	(q, χ_1, χ_2)	\tilde{a}_0	c_3^{newlogs}
13	BBH:0004	(1, -0.50, 0.0)	-0.25	54
14	BBH:0005	(1, +0.50, 0.0)	+0.25	34.5
15	BBH:2105	(1, +0.90, 0.0)	+0.45	27.4
16	BBH:2106	(1, +0.90, +0.50)	+0.70	20.0
17	BBH:0016	(1.5, -0.50, 0.0)	-0.30	53.0
18	BBH:1146	(1.5, +0.95, +0.95)	+0.95	14.5
19	BBH:0552	(1.75, +0.80, -0.40)	+0.36	29
20	BBH:1466	(1.90, +0.70, -0.80)	+0.18	34
21	BBH:2129	(2, +0.60, 0.0)	+0.40	28.5
22	BBH:0258	(2, +0.87, -0.85)	+0.296	29.8
23	BBH:2130	(2, +0.60, +0.60)	+0.60	23
24	BBH:2131	(2, +0.85, +0.85)	+0.85	16.9
25	BBH:1453	(2.352, +0.80, -0.78)	+0.328	29.8
26	BBH:2139	(3, -0.50, -0.50)	-0.50	64
27	BBH:0036	(3, -0.50, 0.0)	-0.38	57
28	BBH:0174	(3, +0.50, 0.0)	+0.37	27.6
29	BBH:2158	(3, +0.50, +0.50)	+0.50	26.8
30	BBH:2163	(3, +0.60, +0.60)	+0.60	24.2
31	BBH:0293	(3, +0.85, +0.85)	+0.85	17.4
32	BBH:0292	(3, +0.73, -0.85)	+0.335	29.5
33	BBH:1447	(3.16, +0.7398, +0.80)	+0.75	19.5
34	BBH:1452	(3.641, +0.80, -0.43)	+0.534	26.5
35	BBH:2014	(4, +0.80, +0.40)	+0.72	21.1
36	BBH:1434	(4.368, +0.7977, +0.7959)	+0.80	18.8
37	BBH:0111	(5, -0.50, 0.0)	-0.42	54
38	BBH:0110	(5, +0.50, 0.0)	+0.42	29.0
39	BBH:1428	(5.516, -0.80, -0.70)	-0.784	79.5
40	BBH:1440	(5.64, +0.77, +0.31)	+0.70	22.5
41	BBH:1432	(5.84, +0.6577, +0.793)	+0.68	23.0
42	BBH:1437	(6.038, +0.80, +0.15)	+0.7076	22.6
43	BBH:1375	(8, -0.90, 0.0)	-0.80	63
44	BBH:1419	(8, -0.80, -0.80)	-0.80	79.0
45	BBH:0114	(8, -0.50, 0.0)	-0.44	60
46	BBH:0065	(8, +0.50, 0.0)	+0.44	25.7
47	BBH:1426	(8, +0.4838, +0.7484)	+0.51	26.5

Except for the $\ell = m = 2$ mode, that is considered at 4PN accuracy following [1] (and is obtained from the factorization of the results of Refs. [48, 49] following [18]), all other modes are hybridized with test-mass information up to 6PN order. The small, though important, change in the analytic treatment of the logarithmic terms is such that our usual approach to NR-inform the model allows a reduction of the EOB/NR differences down to an unprecedented level, with a median EOB/NR unfaithfulness $\mathcal{F}_{\text{EOBNR}}^{\text{median}} = 3.418 \times 10^{-4}$ all over the SXS catalog of 534 quasi-circular, spin-aligned datasets. This is comparable to other quasi-circular models like `TEOBResumS-GIOTTO` [3] and `SEOBNRv5` [40] and better by almost one order of magnitude than the eccentric `SEOBNRv4E` model [50] (compare the middle panel of our Fig. 6 with Fig. 3 of Ref. [50]).

When considering eccentric inspiral configurations, the EOB/NR agreement is generally improved with respect to Paper I (especially for large spins) with $\bar{\mathcal{F}}_{\text{EOBNR}}$ always below 5×10^{-3} , save for the single outlier, SXS:BBH:324, that is however characterized by a rather noisy NR inspiral.

The largest value of $\bar{\mathcal{F}}_{\text{EOBNR}}^{\text{max}}$ that we find for quasi-circular configurations is $\sim 10^{-2}$, and corresponds to $q = 1$, $\chi_1 = \chi_2 = +0.994$, see the rightmost panel of Fig. 6. Notably, just six equal-mass datasets with $\chi_1 = \chi_2 \gtrsim +0.97$ have $\bar{\mathcal{F}}_{\text{EOBNR}}^{\text{max}} > 5 \times 10^{-3}$. These figures correspond to an EOB/NR phase difference at merger as large as ~ 2 rad (for the extreme cases) that is accumulated in the last ~ 10 orbits (see e.g. the top right panel of Fig. 5) and might be due to the interplay between the sub-optimal modelization of the radiation reaction and of spin-orbit effects in the Hamiltonian. As a preliminary investigation, we explored different resummation strategies for the spin-dependent part of the $\ell = m = 2$ factorized waveform amplitude ρ_{22} (including Borel-Padé-Laplace summation) and concluded that the NNLO spin-orbit contribution could be robustly incorporated in resummed form. This statement calls however for a systematic investigation of the properties of the spin-orbit part of the Hamiltonian, going beyond the standard treatment used here (that is still based on Ref. [4]) and building upon some recent, though partly inconclusive, investigations regarding N³LO spin-orbit effects [2] or gauge choices [51].

Note that the median unfaithfulness above for quasi-circular configurations is approximately half of the value $\mathcal{M}^{\text{median}} \sim 6.1 \times 10^{-4}$ obtained by the recent SEOBNR-PM model based on the incorporation of Post Minkowskian information within the EOB approach [52]. Given that our model remains based on resummed PN expansions, but with a more careful analytical treatment, our results seem to suggest that in building EOB-based waveform models the choice of resummation schemes might be somewhat more important than the amount of analytical information incorporated. This could be the case since in both SEOBNR-PM and TEOBResumS-DaLi NR data is used to separately fit functions concerning the nonspinning and spinning sectors, although the analytical structure is different. In particular, we stress that for TEOBResumS-DaLi the NR-calibration is comparatively light, with one function entering the nonspinning sector (a_6^c , Eq. (19)) and one the spinning sector (c_3 , Eq. (20)). A total of 15 NR-informed fitting coefficients, 3 in a_6^c plus 12 in c_3 , are determined using just 51 NR datasets, 4 nonspinning and 47 spinning (see Tables IV-V). This results in the high EOB/NR faithfulness over the entire available SXS catalog described in detail above. Similar accounting applies also for the quasi-circular TEOBResumS-GIOTTO model, notably including the v4.3.2 of Ref. [3]. This should be contrasted with the current SEOB models: 21 NR-fitting parameters, 5 for the nonspinning part and 16 for the spinning part, treated separately through hierarchical fits, enter the Δt_{NR} function used in SEOBNR-PM (Eq. (C1) of Ref. [52]), which parametrizes the distance between the peak of the (2, 2) mode amplitude and the ISCO; 46 parameters (10 nonspinning and 36 spinning) are used in the the SEOBNRv5 model, see Eqs. (78)-(81) of Ref. [40], where four different functions are NR-informed (two for the nonspinning part and two for the spinning part). It is also worth mentioning

that, according to Refs. [40, 52], 441 NR simulations were used to determine the SEOBNR parameters. All considered, TEOBResumS (in either its quasi-circular or eccentric avatars) seems to be able to achieve comparable (or better) performance to both PN-based and PM-based SEOBNR models, while making lighter use of NR calibration. The reason for this is at the moment unclear, but might be related to the different treatment of the flux and radiation reaction.

For scattering configurations, we find an unprecedented EOB/NR agreement ($< 1\%$) for relatively small values of the scattering angle, though differences progressively increase as the threshold of immediate capture is approached³. This is the case for both nonspinning (see Table II) and spinning (see Table III) configurations, thus suggesting that improvements to the conservative dynamics in this part of the binary parameter space are needed. Our findings are also consistent with other recent investigations involving NR simulations at the threshold of immediate capture [43].

In conclusion, we believe that the analysis presented here gives us confidence in the reliability of the dissipative sector of TEOBResumS-DaLi and its resummation. Further improvement in the model is likely to come from a new, more systematic analysis of the conservative sector, possibly including higher-order PN effects in the (D, Q) functions, in the spin-orbit contributions, and attempting new resummation strategies. For example, preliminary analyses concerning the impact of the (resummed) D function at 6PN can be found in Ref. [44] (see Fig. 10 and Table VI therein), while analogous investigations about the mutual compensation of the impact of (D, Q) at different PN orders are discussed in Ref. [3] (see Fig. 6 there). We believe that such a systematic analysis will be key to further increase the EOB/NR faithfulness of TEOBResumS-DaLi all over the parameter space, notably for large, positive, spins and towards the threshold of immediate capture for unbound orbits.

ACKNOWLEDGMENTS

V. F. is supported by the ERC-SyG project ‘‘Recursive and Exact New Quantum Theory’’ (ReNewQuantum), which received funding from the European Research Council (ERC) within the European Union’s Horizon 2020 research and innovation program under Grant No. 810573. S. B. acknowledges support by the EU Horizon under ERC Consolidator Grant, no. InspiReM-101043372. P. R. and S. B. thank the hospitality and the stimulating environment of the IHES, where part of this work was carried out. D.C. acknowledges support from the Italian Ministry of University and Research (MUR) via the PRIN 2022ZHYFA2, *Gravitational waveform models for coalescing compact binaries with eccentricity* (GREAT). The present research was also partly supported by the ‘‘2021 Balzan Prize for Gravitation: Physical and Astrophysical Aspects’’, awarded to Thibault Damour.

³ Note that no quantitative testing on open orbits is currently available for the SEOBNRv4E model [50], but only qualitative results.

Appendix A: Radiation reaction force: structure, implementation and testing

We include in this Appendix a detailed explanation of the implementation of the non-circular radiation reaction model used in `TEOBResumS` and introduced in [11], with particular focus on the matter of the iterative computation of high-order time-derivatives of the dynamical variables.

The `TEOBResumS` radiation reaction model for circularized binaries is based on the special resummation and factorization scheme employed for the multipolar waveform [4, 18]. The angular component entering the equations of motion reads:

$$\hat{\mathcal{F}}_\varphi^{\text{circ}} = -\frac{32}{5}\nu r_\omega^4 \Omega^5 \hat{f}(x), \quad (\text{A1})$$

where the definition of r_ω can be found in Eq. (70) of Ref. [4], $\Omega = \dot{\varphi}$ is the orbital frequency, and $x = r_\omega \Omega = v_\varphi^2$ is computed along the EOB dynamics. Since most of the structure below stems from the quasi-circular limit, where $x = \Omega^{2/3}$, we prefer not to keep x explicit. The factor $\hat{f}(x)$ is a sum of modes $\hat{f}_{\ell m}$, each normalized by the leading-order, $\ell = 2, m = 2$ Newtonian flux $\mathcal{F}_{22}^{\text{Newt}} = -\frac{32}{5}\nu\Omega^{10/3}$, and factorized and resummed following the scheme used for the waveform multipoles, as recalled in Sec. II B of the main text.

When considering generic orbital dynamics, each of these modes can be complemented by an additional non-

circular correcting factor,

$$\hat{f}(\Omega) = \sum_{\ell=2}^8 \sum_{m=-\ell}^{\ell} \hat{f}_{\ell m} \hat{f}_{\ell m}^{\text{non-circular}}, \quad (\text{A2})$$

of which `TEOBResumS` currently uses only the leading-order $(\ell, m) = (2, 2)$ term:

$$\begin{aligned} \hat{f}_{22}^{\text{non-circular}}(r, \Omega; \dot{r}, \dot{\Omega}, \dots) &= 1 + \frac{3}{4} \frac{\dot{r}^2}{r^2 \Omega^4} - \frac{\ddot{\Omega}}{4 \Omega^3} + \frac{3 \dot{r} \dot{\Omega}}{r \Omega^3} \\ &+ \frac{4 \dot{r}^2}{r^2 \Omega^2} + \frac{\ddot{\Omega} \dot{r}^2}{8 r^2 \Omega^5} + \frac{3 \dot{r}^3 \dot{\Omega}}{4 r^3 \Omega^5} + \frac{3 \dot{r}^4}{4 r^4 \Omega^4} + \frac{3 \dot{\Omega}^2}{4 \Omega^4} \\ &- \ddot{r} \left(\frac{\dot{r}}{2 r^2 \Omega^4} + \frac{\dot{\Omega}}{8 r \Omega^5} \right) + \ddot{r} \left(-\frac{2}{r \Omega^2} + \frac{\ddot{\Omega}}{8 r \Omega^5} + \frac{3 \dot{r} \dot{\Omega}}{8 r^2 \Omega^5} \right). \end{aligned} \quad (\text{A3})$$

As this equation shows, the noncircular correcting factor depends not only on the phase space coordinates, but also on their time-derivatives (up to the third-order). In principle, these can be straightforwardly determined (irrespective of their algebraic complexity) by consecutive derivatives of the Hamiltonian. For instance, consider the case of the orbital frequency. Following the notation of Ref. [2], Hamilton's equation for φ reads:

$$\Omega = \dot{\varphi} = \frac{\partial \hat{H}_{\text{EOB}}}{\partial p_\varphi} = \frac{p_\varphi A u_c^2}{\nu \hat{H}_{\text{EOB}} \hat{H}_{\text{eff}}^{\text{orb}}} + \frac{\tilde{G}(r_c, p_{r_*}, p_\varphi)}{\nu \hat{H}_{\text{EOB}}} \quad (\text{A4})$$

By further differentiating this expression, one finds:

$$\begin{aligned} \dot{\Omega} &= \frac{1}{\nu \hat{H}_{\text{EOB}} \hat{H}_{\text{eff}}^{\text{orb}}} \left[\left(A u_c^2 \right)' p_\varphi \dot{r} + A u_c^2 \left(\dot{p}_\varphi - p_\varphi \frac{1}{\nu \hat{H}_{\text{EOB}} \hat{H}_{\text{eff}}^{\text{orb}}} \frac{d}{dt} \left(\nu \hat{H}_{\text{EOB}} \hat{H}_{\text{eff}}^{\text{orb}} \right) \right) \right] \\ &+ \frac{1}{\nu \hat{H}_{\text{EOB}}} \left[\tilde{G}' \dot{r} + \frac{\partial \tilde{G}}{\partial p_{r_*}} \dot{p}_{r_*} - \tilde{G} \frac{\dot{\hat{H}}_{\text{EOB}}}{\hat{H}_{\text{EOB}}} \right], \end{aligned} \quad (\text{A5})$$

where a prime denotes differentiation with respect to r . All other time-derivatives of the dynamical variables can be computed in a similar fashion. Notice, however, that the above equation contains time-derivatives of p_φ and of the energy \hat{H}_{EOB} . These terms would vanish in the conservative problem. Here, however, they are non-zero and are entirely due to the radiation reaction terms:

$$\dot{p}_\varphi = \hat{\mathcal{F}}_\varphi, \quad (\text{A6})$$

$$\dot{\hat{H}}_{\text{EOB}} = \dot{r} \hat{\mathcal{F}}_r + \Omega \hat{\mathcal{F}}_\varphi, \quad (\text{A7})$$

where the equation for $\dot{\hat{H}}_{\text{EOB}}$ is a consequence of the structure of Hamilton's equations modified by the dissipative terms; cfr. Eq. (2.4) of Ref. [53]. Since these expressions enter the $(2, 2)$ prefactor in the angular flux itself, the equation defining $\hat{\mathcal{F}}_\varphi$ is actually a non-trivial nonlinear one (not to mention the fact that the time derivatives of $\hat{\mathcal{F}}_\varphi$ show up as well in, e.g., $\ddot{r}, \ddot{\Omega}$).

In order to more simply and efficiently compute the full angular radiation reaction, we resort to an approximate iterative method that generalizes the one introduced in

Ref. [54] to calculate \ddot{r} for the determination of the non-quasi-circular (NQC) corrections to the waveform.

First approximations to the necessary time derivatives are computed by using as a “0th order” value $\hat{\mathcal{F}}_\varphi^{(0)}$ the circularized prescription, excluding the $(2, 2)$ Newtonian prefactor; with these, a first solution for the full $\hat{\mathcal{F}}_\varphi$ is calculated.

Denoting generically by z the time derivatives of the dynamical variables r, Ω , we have:

$$z^{(0)} \equiv z(r, p_{r_*}, p_\varphi; \hat{\mathcal{F}}_\varphi^{(0)} \equiv \hat{\mathcal{F}}_\varphi^{\text{circ}}), \quad (\text{A8})$$

$$\hat{\mathcal{F}}_\varphi^{(1)} \equiv -\frac{32}{5} \nu r_\omega^4 \Omega^5 \hat{f}(\Omega; z^{(0)}), \quad (\text{A9})$$

where we highlighted in the Newton-normalized flux function \hat{f} dependence on the z through the Newtonian prefactor of Eq. (A3). Better approximations of the z are then computed using $\hat{\mathcal{F}}_\varphi^{(1)}$ as angular radiation reaction. With

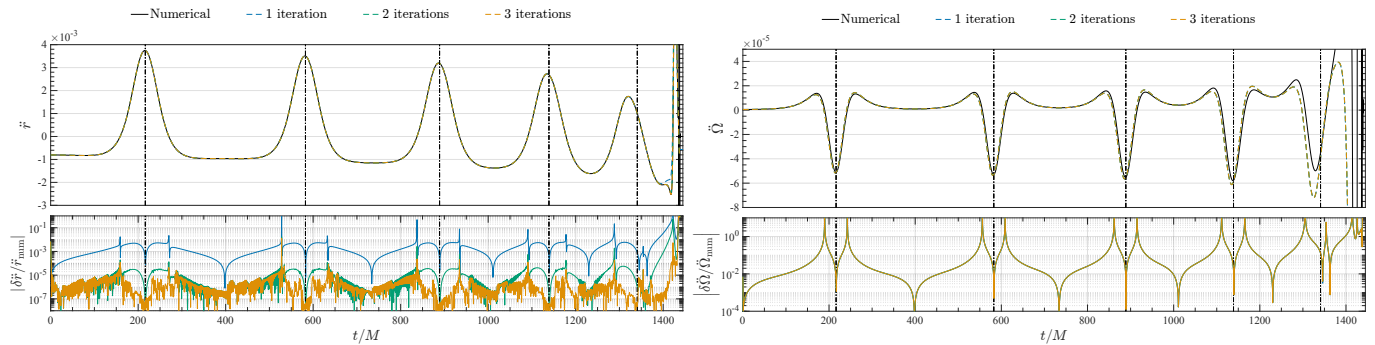


FIG. 8. Comparisons between \ddot{r} and $\ddot{\Omega}$ as calculated by numerically differentiating the dynamics with a 4th order scheme and using the iterative procedure, with up to 3 iterations, for an equal-mass system with $\chi_1 = \chi_2 = 0.6$ and initial eccentricity 0.5. Direct comparisons in the top panels, and relative differences between analytical and numerical values in the bottom panels. Vertical lines mark periastron passages. Convergence is evident in the case of \ddot{r} ; as mentioned in the test, neglected terms in its analytical expression cause errors larger than between successive iterations in the case of $\ddot{\Omega}$.

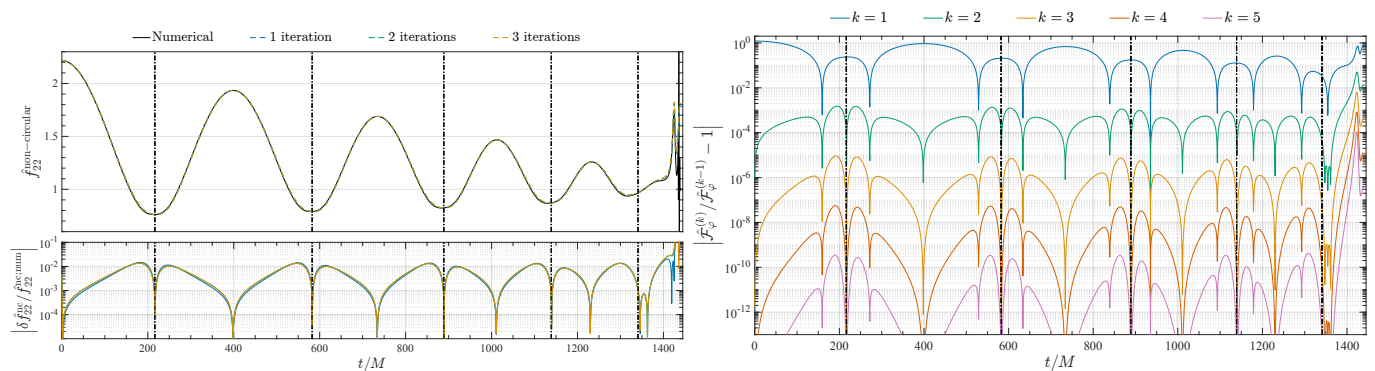


FIG. 9. Left panel: the first three iterations of the non-circular correcting factor $\hat{f}_{22}^{\text{non-circular}}$ for the same system parameters considered in Fig. 8. The iterative results are compared with the prefactor calculated using numerical derivatives of r and Ω . Relative differences exceed the 10^{-2} level only at the very end of the dynamics. Right panel: convergence of the complete angular radiation reaction, shown through the relative difference between the result of each iteration and the previous one. Any iteration beyond the second causes changes below the 0.01% level in the complete flux.

them, a second-order solution for $\hat{\mathcal{F}}_\varphi$ is found:

$$z^{(1)} \equiv z(r, p_{r_*}, p_\varphi; \hat{\mathcal{F}}_\varphi^{(1)}) \quad (\text{A10})$$

$$\hat{\mathcal{F}}_\varphi^{(2)} \equiv -\frac{32}{5} \nu r_\omega^4 \Omega^5 \hat{f}(\Omega; z^{(1)}). \quad (\text{A11})$$

This procedure can then be iterated for better approximations to the correct solution, with convergence tests carried out by comparing the iterated time-derivatives with those found through numerical differentiation of the output of the integration of the dynamics. We neglect any time-derivative of the radiation reaction components themselves, which appear in the third-order derivatives, \ddot{p}_{r_*} , \ddot{r} , and $\ddot{\Omega}$.

Performing the aforementioned tests in the comparable mass case, where radiation reaction is strongest, we found that two iterations (i.e., going up to $\hat{\mathcal{F}}_\varphi^{(2)}$) should be enough for our purposes. In all cases, looking at either the actual time-derivatives of the dynamical variables, the Newtonian prefactor, or the flux itself, the iteration converges quite fast, with negligible variations already above three loops. In particular, the iterated second-order time-derivatives (\ddot{r} , $\ddot{\Omega}$) excellently reproduce the numerical exact ones from the second iteration onward (with a relative error $\lesssim 10^{-4}$ during the inspiral, only exceeding that threshold in the last moments before merger).

When looking at third-order derivatives, \ddot{p}_{r_*} , \ddot{r} , $\ddot{\Omega}$, the neglected terms in their analytical expressions prevent similarly precise recovery of their exact values; indeed, differences between consecutive iterations quickly fall below the weight of the missing terms. As a consequence, even during the inspiral, relative differences between the exact numerical derivatives and those found through two iterations can peak above $\sim 10^{-1}$. Of those mentioned above, $\ddot{\Omega}$ seems to be the one most suffering from the neglected terms, especially at the end of the inspiral and during plunge.

However, these inaccuracies still have little impact on the Newtonian prefactor, and as such on the flux. At two iterations, the analytical $\hat{f}_{22}^{\text{non-circular}}$ reproduces the correcting factor as computed using numerical derivatives of the dynamical variables to within 10^{-2} relative accuracy throughout the inspiral. This is true in all cases but those with very high, positive spins and/or high eccentricity, where inaccuracies still don't exceed $\sim 2 \cdot 10^{-2}$ in relative terms. Fig. 9 shows in an example system how any iteration beyond the second produces extremely small corrections to the complete angular radiation reaction \mathcal{F}_φ , below 0.01% throughout the inspiral, justifying our choice of stopping at two iterations.

In conclusion, the iterative procedure outlined in this Appendix converges fast, producing very accurate results

for some of the required time-derivatives ($\ddot{r}, \dot{\Omega}$). Relatively high inaccuracies do remain in some cases due to neglected terms in the analytical expressions containing derivatives of the radiation reaction, but their effect on the non-circular correcting factor and the angular flux remains small, and mostly confined to the very late stages

of the binary evolution, at or around plunge, where the conservative dynamics dominates. It should also be mentioned that the kind of effect that such small variations in the radiation reaction can have on the dynamics in this phase of the evolution is of the order of magnitude of what is ordinarily corrected through NR calibration.

-
- [1] A. Nagar, R. Gamba, P. Rettegno, V. Fantini, and S. Bernuzzi, Effective-one-body waveform model for non-circularized, planar, coalescing black hole binaries: the importance of radiation reaction, (2024), [arXiv:2404.05288 \[gr-qc\]](#).
- [2] A. Nagar and P. Rettegno, Next generation: Impact of high-order analytical information on effective one body waveform models for noncircularized, spin-aligned black hole binaries, *Phys. Rev. D* **104**, 104004 (2021), [arXiv:2108.02043 \[gr-qc\]](#).
- [3] A. Nagar, P. Rettegno, R. Gamba, S. Albanesi, A. Albertini, and S. Bernuzzi, Analytic systematics in next generation of effective-one-body gravitational waveform models for future observations, *Phys. Rev. D* **108**, 124018 (2023), [arXiv:2304.09662 \[gr-qc\]](#).
- [4] T. Damour and A. Nagar, New effective-one-body description of coalescing nonprecessing spinning black-hole binaries, *Phys. Rev. D* **90**, 044018 (2014), [arXiv:1406.6913 \[gr-qc\]](#).
- [5] A. Nagar et al., Time-domain effective-one-body gravitational waveforms for coalescing compact binaries with nonprecessing spins, tides and self-spin effects, *Phys. Rev. D* **98**, 104052 (2018), [arXiv:1806.01772 \[gr-qc\]](#).
- [6] A. Albertini, A. Nagar, A. Pound, N. Warburton, B. Wardell, L. Durkan, and J. Miller, Comparing second-order gravitational self-force, numerical relativity, and effective one body waveforms from inspiralling, quasicircular, and nonspinning black hole binaries, *Phys. Rev. D* **106**, 084061 (2022), [arXiv:2208.01049 \[gr-qc\]](#).
- [7] A. Albertini, A. Nagar, A. Pound, N. Warburton, B. Wardell, L. Durkan, and J. Miller, Comparing second-order gravitational self-force and effective one body waveforms from inspiralling, quasicircular and nonspinning black hole binaries. II. The large-mass-ratio case, *Phys. Rev. D* **106**, 084062 (2022), [arXiv:2208.02055 \[gr-qc\]](#).
- [8] A. Albertini, R. Gamba, A. Nagar, and S. Bernuzzi, Effective-one-body waveforms for extreme-mass-ratio binaries: Consistency with second-order gravitational self-force quasicircular results and extension to nonprecessing spins and eccentricity, *Phys. Rev. D* **109**, 044022 (2024), [arXiv:2310.13578 \[gr-qc\]](#).
- [9] A. Albertini, A. Nagar, J. Mathews, and G. Lukes-Gerakopoulos, Comparing second-order gravitational self-force and effective-one-body waveforms from inspiralling, quasi-circular black hole binaries with a non-spinning primary and a spinning secondary, (2024), [arXiv:2406.04108 \[gr-qc\]](#).
- [10] R. Gamba, D. Chiaramello, and S. Neogi, Towards efficient Effective One Body models for generic, non-planar orbits, (2024), [arXiv:2404.15408 \[gr-qc\]](#).
- [11] D. Chiaramello and A. Nagar, Faithful analytical effective-one-body waveform model for spin-aligned, moderately eccentric, coalescing black hole binaries, *Phys. Rev. D* **101**, 101501 (2020), [arXiv:2001.11736 \[gr-qc\]](#).
- [12] A. Nagar and A. Shah, Factorization and resummation: A new paradigm to improve gravitational wave amplitudes, *Phys. Rev. D* **94**, 104017 (2016), [arXiv:1606.00207 \[gr-qc\]](#).
- [13] Q. Henry, S. Marsat, and M. Khalil, Spin contributions to the gravitational-waveform modes for spin-aligned binaries at the 3.5PN order, *Phys. Rev. D* **106**, 124018 (2022), [arXiv:2209.00374 \[gr-qc\]](#).
- [14] A. Bohé et al., Improved effective-one-body model of spinning, nonprecessing binary black holes for the era of gravitational-wave astrophysics with advanced detectors, *Phys. Rev. D* **95**, 044028 (2017), [arXiv:1611.03703 \[gr-qc\]](#).
- [15] F. Messina, A. Maldarella, and A. Nagar, Factorization and resummation: A new paradigm to improve gravitational wave amplitudes. II: the higher multipolar modes, *Phys. Rev. D* **97**, 084016 (2018), [arXiv:1801.02366 \[gr-qc\]](#).
- [16] D. Bini, T. Damour, and A. Gericco, Novel approach to binary dynamics: application to the fifth post-Newtonian level, *Phys. Rev. Lett.* **123**, 231104 (2019), [arXiv:1909.02375 \[gr-qc\]](#).
- [17] D. Bini, T. Damour, and A. Gericco, Binary dynamics at the fifth and fifth-and-a-half post-Newtonian orders, *Phys. Rev. D* **102**, 024062 (2020), [arXiv:2003.11891 \[gr-qc\]](#).
- [18] T. Damour, B. R. Iyer, and A. Nagar, Improved resummation of post-Newtonian multipolar waveforms from circularized compact binaries, *Phys. Rev. D* **79**, 064004 (2009), [arXiv:0811.2069 \[gr-qc\]](#).
- [19] R. Fujita and B. R. Iyer, Spherical harmonic modes of 5.5 post-Newtonian gravitational wave polarizations and associated factorized resummed waveforms for a particle in circular orbit around a Schwarzschild black hole, *Phys. Rev. D* **82**, 044051 (2010), [arXiv:1005.2266 \[gr-qc\]](#).
- [20] S. Albanesi, A. Nagar, and S. Bernuzzi, Effective one-body model for extreme-mass-ratio spinning binaries on eccentric equatorial orbits: Testing radiation reaction and waveform, *Phys. Rev. D* **104**, 024067 (2021), [arXiv:2104.10559 \[gr-qc\]](#).
- [21] M. Panzeri, V. Fantini, and A. Nagar, in preparation, (2024).
- [22] C. Mitschi and D. Sauzin, [Divergent series, summability and resurgence. I](#), Lecture Notes in Mathematics, Vol. 2153 (Springer, [Cham], 2016) pp. xxi+298, monodromy and resurgence, With a foreword by Jean-Pierre Ramis and a preface by Éric Delabaere, Michèle Loday-Richaud, Claude Mitschi and David Sauzin.
- [23] O. Costin, [Asymptotics and Borel summability](#), Chapman & Hall/CRC Monographs and Surveys in Pure and Applied Mathematics, Vol. 141 (CRC Press, Boca Raton, FL, 2009) pp. xiv+250.
- [24] V. Fantini and C. Rella, Strong-weak symmetry and quantum modularity of resurgent topological strings on local \mathbb{P}^2 , (2024), [arXiv:2404.10695 \[hep-th\]](#).
- [25] S. Hild, S. Chelkowski, and A. Freise, Pushing towards the ET sensitivity using 'conventional' technology, (2008), [arXiv:0810.0604 \[gr-qc\]](#).
- [26] S. Hild, S. Chelkowski, A. Freise, J. Franc, N. Morgado, R. Flaminio, and R. DeSalvo, A Xylophone Configuration for a third Generation Gravitational Wave Detector, *Class. Quant. Grav.* **27**, 015003 (2010), [arXiv:0906.2655 \[gr-qc\]](#).
- [27] S. Hild et al., Sensitivity Studies for Third-Generation Gravitational Wave Observatories, *Class. Quant. Grav.* **28**, 094013 (2011), [arXiv:1012.0908 \[gr-qc\]](#).
- [28] Updated Advanced LIGO sensitivity design curve, <https://>

- [//dcc.ligo.org/LIGO-T1800044/public](https://dcc.ligo.org/LIGO-T1800044/public).
- [29] T. Damour, F. Guercilena, I. Hinder, S. Hopper, A. Nagar, and L. Rezzolla, Strong-Field Scattering of Two Black Holes: Numerics Versus Analytics, *Phys. Rev. D* **89**, 081503 (2014), [arXiv:1402.7307 \[gr-qc\]](https://arxiv.org/abs/1402.7307).
- [30] S. Hopper, A. Nagar, and P. Rettegnò, Strong-field scattering of two spinning black holes: Numerics versus analytics, *Phys. Rev. D* **107**, 124034 (2023), [arXiv:2204.10299 \[gr-qc\]](https://arxiv.org/abs/2204.10299).
- [31] P. Rettegnò, G. Pratten, L. M. Thomas, P. Schmidt, and T. Damour, Strong-field scattering of two spinning black holes: Numerical relativity versus post-Minkowskian gravity, *Phys. Rev. D* **108**, 124016 (2023), [arXiv:2307.06999 \[gr-qc\]](https://arxiv.org/abs/2307.06999).
- [32] A. Nagar and L. Rezzolla, Gauge-invariant non-spherical metric perturbations of Schwarzschild black-hole spacetimes, *Class. Quant. Grav.* **22**, R167 (2005), [arXiv:gr-qc/0502064](https://arxiv.org/abs/gr-qc/0502064).
- [33] M. Boyle et al., The SXS Collaboration catalog of binary black hole simulations, *Class. Quant. Grav.* **36**, 195006 (2019), [arXiv:1904.04831 \[gr-qc\]](https://arxiv.org/abs/1904.04831).
- [34] A. Nagar, G. Riemenschneider, G. Pratten, P. Rettegnò, and F. Messina, Multipolar effective one body waveform model for spin-aligned black hole binaries, *Phys. Rev. D* **102**, 024077 (2020), [arXiv:2001.09082 \[gr-qc\]](https://arxiv.org/abs/2001.09082).
- [35] C. O. Lousto and J. Healy, Exploring the Small Mass Ratio Binary Black Hole Merger via Zeno's Dichotomy Approach, *Phys. Rev. Lett.* **125**, 191102 (2020), [arXiv:2006.04818 \[gr-qc\]](https://arxiv.org/abs/2006.04818).
- [36] A. Nagar, J. Healy, C. O. Lousto, S. Bernuzzi, and A. Albertini, Numerical-relativity validation of effective-one-body waveforms in the intermediate-mass-ratio regime, *Phys. Rev. D* **105**, 124061 (2022), [arXiv:2202.05643 \[gr-qc\]](https://arxiv.org/abs/2202.05643).
- [37] S. Taylor and E. Poisson, Nonrotating black hole in a post-Newtonian tidal environment, *Phys. Rev. D* **78**, 084016 (2008), [arXiv:0806.3052 \[gr-qc\]](https://arxiv.org/abs/0806.3052).
- [38] K. Chatziioannou, E. Poisson, and N. Yunes, Tidal heating and torquing of a Kerr black hole to next-to-leading order in the tidal coupling, *Phys. Rev. D* **87**, 044022 (2013), [arXiv:1211.1686 \[gr-qc\]](https://arxiv.org/abs/1211.1686).
- [39] M. V. S. Saketh, J. Steinhoff, J. Vines, and A. Buonanno, Modeling horizon absorption in spinning binary black holes using effective worldline theory, *Phys. Rev. D* **107**, 084006 (2023), [arXiv:2212.13095 \[gr-qc\]](https://arxiv.org/abs/2212.13095).
- [40] L. Pompili et al., Laying the foundation of the effective-one-body waveform models SEOBNRv5: improved accuracy and efficiency for spinning non-precessing binary black holes, (2023), [arXiv:2303.18039 \[gr-qc\]](https://arxiv.org/abs/2303.18039).
- [41] I. Hinder, L. E. Kidder, and H. P. Pfeiffer, An eccentric binary black hole inspiral-merger-ringdown gravitational waveform model from numerical relativity and post-Newtonian theory, (2017), [arXiv:1709.02007 \[gr-qc\]](https://arxiv.org/abs/1709.02007).
- [42] A. Bonino, P. Schmidt, and G. Pratten, Mapping eccentricity evolutions between numerical relativity and effective-one-body gravitational waveforms, (2024), [arXiv:2404.18875 \[gr-qc\]](https://arxiv.org/abs/2404.18875).
- [43] S. Albanesi, A. Rashti, F. Zappa, R. Gamba, W. Cook, B. Daszuta, S. Bernuzzi, A. Nagar, and D. Radice, Scattering and dynamical capture of two black holes: synergies between numerical and analytical methods, (2024), [arXiv:2405.20398 \[gr-qc\]](https://arxiv.org/abs/2405.20398).
- [44] A. Nagar, P. Rettegnò, R. Gamba, and S. Bernuzzi, Effective-one-body waveforms from dynamical captures in black hole binaries, *Phys. Rev. D* **103**, 064013 (2021), [arXiv:2009.12857 \[gr-qc\]](https://arxiv.org/abs/2009.12857).
- [45] M. Pürrer and C.-J. Haster, Gravitational waveform accuracy requirements for future ground-based detectors, *Phys. Rev. Res.* **2**, 023151 (2020), [arXiv:1912.10055 \[gr-qc\]](https://arxiv.org/abs/1912.10055).
- [46] V. Kapil, L. Reali, R. Cotesta, and E. Berti, Systematic bias from waveform modeling for binary black hole populations in next-generation gravitational wave detectors, *Phys. Rev. D* **109**, 104043 (2024), [arXiv:2404.00090 \[gr-qc\]](https://arxiv.org/abs/2404.00090).
- [47] A. Dhani, S. Völkel, A. Buonanno, H. Estelles, J. Gair, H. P. Pfeiffer, L. Pompili, and A. Toubiana, Systematic Biases in Estimating the Properties of Black Holes Due to Inaccurate Gravitational-Wave Models, (2024), [arXiv:2404.05811 \[gr-qc\]](https://arxiv.org/abs/2404.05811).
- [48] L. Blanchet, G. Faye, Q. Henry, F. Larrouturou, and D. Trestini, Gravitational-Wave Phasing of Quasicircular Compact Binary Systems to the Fourth-and-a-Half Post-Newtonian Order, *Phys. Rev. Lett.* **131**, 121402 (2023), [arXiv:2304.11185 \[gr-qc\]](https://arxiv.org/abs/2304.11185).
- [49] L. Blanchet, G. Faye, Q. Henry, F. Larrouturou, and D. Trestini, Gravitational-wave flux and quadrupole modes from quasicircular nonspinning compact binaries to the fourth post-Newtonian order, *Phys. Rev. D* **108**, 064041 (2023), [arXiv:2304.11186 \[gr-qc\]](https://arxiv.org/abs/2304.11186).
- [50] A. Ramos-Buades, A. Buonanno, M. Khalil, and S. Ossokine, Effective-one-body multipolar waveforms for eccentric binary black holes with nonprecessing spins, *Phys. Rev. D* **105**, 044035 (2022), [arXiv:2112.06952 \[gr-qc\]](https://arxiv.org/abs/2112.06952).
- [51] A. Placidi, P. Rettegnò, and A. Nagar, Gravitational spin-orbit coupling through the third-subleading post-Newtonian order: exploring spin-gauge flexibility, (2024), [arXiv:2401.12290 \[gr-qc\]](https://arxiv.org/abs/2401.12290).
- [52] A. Buonanno, G. Mogull, R. Patil, and L. Pompili, Post-Minkowskian Theory Meets the Spinning Effective-One-Body Approach for Bound-Orbit Waveforms, (2024), [arXiv:2405.19181 \[gr-qc\]](https://arxiv.org/abs/2405.19181).
- [53] D. Bini and T. Damour, Gravitational radiation reaction along general orbits in the effective one-body formalism, *Phys. Rev. D* **86**, 124012 (2012), [arXiv:1210.2834 \[gr-qc\]](https://arxiv.org/abs/1210.2834).
- [54] T. Damour, A. Nagar, and S. Bernuzzi, Improved effective-one-body description of coalescing nonspinning black-hole binaries and its numerical-relativity completion, *Phys. Rev. D* **87**, 084035 (2013), [arXiv:1212.4357 \[gr-qc\]](https://arxiv.org/abs/1212.4357).